Fabrication of a snail shell-like structured MnO₂@CoNiO₂ composite electrode for high performance supercapacitors

Araveeti Eswar Reddy, Tarugu Anitha, Chandu V. V. M. Gopi, S. Srinivasa Rao, Chebrolu Venkata Thulasi-Varma, Dinah Punnoose and Hee-Je Kim*

For the first time, we develop a cost-effective and facile one-step hydrothermal approach to directly grow MnO_2@$CoNiO_2$ snail shell-like, $CoNiO_2$ nanoflake-like, and MnO_2 nanoflower-like structures on nickel foam as electrode for supercapacitor applications. Cyclic voltammetry, galvanostatic charge–discharge cycling, and electrochemical impedance spectroscopy are used to investigate the electrochemical responses of the electrodes. The MnO_2@$CoNiO_2$ composite electrode exhibits a high specific capacitance and energy density of 1605.4 F g^{-1} and 51.37 W h kg^{-1}, respectively, at 20 mA cm^{-2} in 3 M KOH aqueous solution, as well as an attractive cycling ability (98.87% even after 3000 cycles at 40 mA cm^{-2}), which are much better than those of the $CoNiO_2$ and MnO_2 electrodes. Such superior electrochemical performance of the MnO_2@$CoNiO_2$ electrode is attributed to the combination of two active materials with an improved surface morphology, which can offer more pathways for electron transport and enhance the utilization of the electrode materials. These results show that the MnO_2@$CoNiO_2$ composites are promising positive electrode materials for practical supercapacitors.

1. Introduction

Lightweight, high performance, excellent reversibility, stability, safety, and environmentally friendly energy storage devices, such as supercapacitors (SCs) and lithium-ion batteries, are required in the present modern electronic industry.[1,2] Lithium-ion batteries (LIBS) and supercapacitors (SCs) have attracted considerable worldwide attention. SCs, also called ultra-capacitors or electrochemical capacitors (ECs), are considered as a new class of electrochemical energy storage devices because they can achieve higher energy density and power density when compared to traditional capacitors and batteries.[3-8] Supercapacitors (SCs) have attracted increasing attention due to their simple principle, fast recharge ability, long cycle life, high power performance, and low maintenance cost,[9,10] which allows applications for a range of power and energy necessities, such as short-term power sources for mobile electronic devices, hybrid electric vehicles, *etc.*[11,12]

SCs can be classified into two categories, pseudo capacitors and electrical double-layer capacitors (EDLCs), according to the electrochemical storage mechanism. Typically, pseudo capacitors have a much larger energy density and higher specific capacitance than EDLCs due to the reversible faradaic redox reactions at the electrode surface.[13-15] Many different materials

and its systems have been studied widely as active electrode materials for SCs because of their higher theoretical specific capacitance.[16-18] Transition metal oxides/hydroxides, carbonaceous materials, and conducting polymers are commonly used materials for supercapacitor applications.[19-26] Among them, transition metal oxides usually offer good electrical performance because of their increased conductivity and their synergic effects.[27,28] Transition metal oxides, such as RuO_2, V_2O_5, NiO, MoO_3, $NiCo_2O_4$, Co_3O_4, TiO_2, SnO_2, and MnO_2,[27-40] have been studied as an attractive electrode material for SCs. Moreover, the electrochemical performance, natural abundance, low cost, and environmental friendliness of MnO_2 makes it a promising candidate for supercapacitor electrodes.[41-44] Recently, many literatures about the fabrication and its super capacitive behavior of $NiCo_2O_4$ have been investigated, such as nanoflakes, nanoparticles, nanowires and flowers.[45-48] The use of both metals in this way enhances electronic conductivity with a reduction in the ternary metal oxides, and is beneficial to electrochemical applications.[49] However, there have been very few studies on the synthesis and supercapacitor evaluation of $CoNiO_2$ due to the lack of feasible fabrication methods without the use of poisonous and noxious reagents to realize mass production.[50,51] Therefore, simple and scalable preparation routes for MnO_2 and $CoNiO_2$ should be investigated to achieve various structure designs of MnO_2 and $CoNiO_2$ nanomaterials with different morphologies for practical applications and supercapacitor performance is unsatisfactory.[52,53] Therefore

School of Electrical Engineering, Pusan National University, Busandaehak-ro 63beon-gil, Geumjeong-gu, Busan, 46241, South Korea. E-mail: heeje@pusan.ac.kr; Fax: +82 51 513 0212; Tel: +82 51 510 2364

composites were developed to improve the electrochemical performance of supercapacitors.

Currently, composites containing oxides have been studied most widely. First-rate supercapacitor electrode materials, such as CNT@MnO_2, CuO@MnO_2, Co_3O_4/SnO_2@MnO_2, TiO_2@MnO_2, $ZnCo_2O_4$@Ni, ZnO@Ni_3S_2, ZnO@$MnCo_2O_4$, Fe_3O_4@Fe_2O_3, Co_3O_4@MnO_2, Fe_3O_4@MnO_2, and $ZnCoO_4$@MnO_2,[54–64] have attracted considerable attention. Recently, Yu et al. developed $NiCo_2O_4$@MnO_2 integrated electrode for high-performance supercapacitors.[65] Impressively, the Ni foam-supported core–shell heterostructured NW array electrode ($NiCo_2O_4$@MnO_2) delivers higher area specific capacitance of 3.31 F cm^{-2} at current density of 2 mA cm^{-2}. On the other hand, there are no reports on the electrochemical capacitance of their integrated materials with the aim of elevating the supercapacitor performance by rationally combining $CoNiO_2$ and MnO_2, even though the individual capacitive behavior of both has been demonstrated.

In this study, a low cost and facile strategy was developed for the design and fabrication of novel hierarchical MnO_2@$CoNiO_2$ nanotube arrays on nickel foam using a facile hydrothermal pathway for supercapacitor applications. This hybrid nanotube arrays delivered a high specific capacitance of 1605.4 F g^{-1}, and operated at a high power density of 1142.75 W kg^{-1} with an energy density of 51.37 W h kg^{-1} at a current density of 20 mA cm^{-2}. These interesting results highlights the potential of MnO_2@$CoNiO_2$ supercapacitors as a high performance energy storage system for practical applications.

2. Experimental section

2.1 Materials

All chemicals, such as manganese(II) nitrate tetrahydrate [$Mn(NO_3)_2 \cdot 4H_2O$], cobalt(II) nitrate hexahydrate [$Co(NO_3)_2 \cdot 6H_2O$], nickel(II) sulfate hexahydrate [$NiSO_4 \cdot 6H_2O$], ammonium fluoride [NH_4F], urea [CH_4N_2O], potassium hydroxide [KOH], and nickel (Ni) foam were purchased from Sigma-Aldrich and used as received.

2.2 Synthesis of MnO_2, $CoNiO_2$ and MnO_2@$CoNiO_2$ electrodes

In a typical procedure, a piece of Ni foam was cut into 1 × 1 cm^2 squares and cleaned ultrasonically in a 2 M HCl solution for 30 minutes. The Ni foams were then cleaned sequentially in acetone, ethanol, and DI water for 15 min each. For the synthesis of the MnO_2@$CoNiO_2$ electrode, 0.702 g (0.04 M) of $Mn(NO_3)_2 \cdot 4H_2O$, 0.814 g (0.04 M) of $Co(NO_3)_2 \cdot 6H_2O$, and 0.735 g (0.04 M) of $NiSO_4 \cdot 6H_2O$ were dispersed in 70 ml of DI water and stirred vigorously for 30 min to form a homogeneous solution. Subsequently, 0.622 g (0.24 M) of NH_4F and 2.018 g (0.48 M) of CH_4N_2O were added sequentially to the above homogeneous solution. After stirring for 30 minutes, the solution was poured into a 100 ml polytetrafluoroethylene (PTFE) Teflon-lined stainless steel autoclave and the pretreated Ni foam was dipped into the reaction mixture. The autoclave was sealed and maintained at 100 °C for 6 h, and cooled naturally to

27 °C. The as-gained Ni foam was removed, washed with DI water, and dried in the oven. Finally, MnO_2@$CoNiO_2$ electrode was obtained by annealing the sample at 200 °C for 2 h in air. $CoNiO_2$ and MnO_2 electrodes were also prepared using the above procedure with the relevant chemicals. The loading of the MnO_2@$CoNiO_2$, $CoNiO_2$, and MnO_2 samples was approximately 4.2, 3.6, and 3.0 mg cm^{-2}, respectively.

2.3 Materials characterization

The morphology of the films was analyzed by field emission scanning electron microscopy (FE-SEM, S-2400, Hitachi) equipped with energy-dispersive X-ray spectroscopy (EDX) operated at 15 kV. The crystalline nature and structure of the electrodes were studied by X-ray diffraction (XRD) analysis on a D8 ADVANCE with a diffractometer using a Cu Kα radiation source operated at 40 kV and 40 mA in the 2θ range of 20–80°. X-ray photon electron spectroscopy (XPS, VG Scientific ESCALAB 250) was performed using monochromatic Al-K$_\alpha$ radiation at 1486.6 eV. Brunauer–Emmett–Teller (BET) analysis was used to measure the specific surface area of the samples using a BEL-sorp-Max (BEL, Japan) instrument at 77 K.

2.4 Electrochemical measurements

All electrochemical characterizations were conducted in a three-electrode configuration consisting of MnO_2 (or $CoNiO_2$ or MnO_2@$CoNiO_2$), Pt wire, and Ag/AgCl as the working electrode, counter electrode, and reference electrode, respectively. The supporting electrolyte consisted of a 3 M KOH aqueous solution. Cyclic voltammetry (CV), galvanostatic charge–discharge tests, and electrochemical impedance spectroscopy (EIS) were measured using a Biologic-SP150 workstation. CV was studied at a potential range from +0.0 V to +0.5 V at 5 mV s^{-1} to 100 mV s^{-1} scan rates. The galvanostatic charge–discharge tests were studied by chronopotentiometry at a voltage window of +0.0 V to +0.48 V at different current densities (20–100) mA cm^{-2}. Electrochemical impedance spectroscopy (EIS) was conducted over a frequency region from 0.1 Hz to 500 kHz. The specific capacitance (C_s, F g^{-1}), energy density (E, W h kg^{-1}), and power density (P, W kg^{-1}) were calculated from the galvanostatic charge–discharge curves using the following equations:[66,67]

$$C_s = \frac{I \times t}{m \times V} \tag{1}$$

$$E = \frac{C_s \times (\Delta V^2)}{2} \tag{2}$$

$$P = \frac{E}{t} \tag{3}$$

where I is the discharge current, t is the discharge time, V is the potential window and m is the mass of the active material.

3. Results and discussion

The morphology and composition of the precursor samples were analyzed by low and high magnification FE-SEM. Fig. 1 presents the morphology of the MnO_2, $CoNiO_2$, and
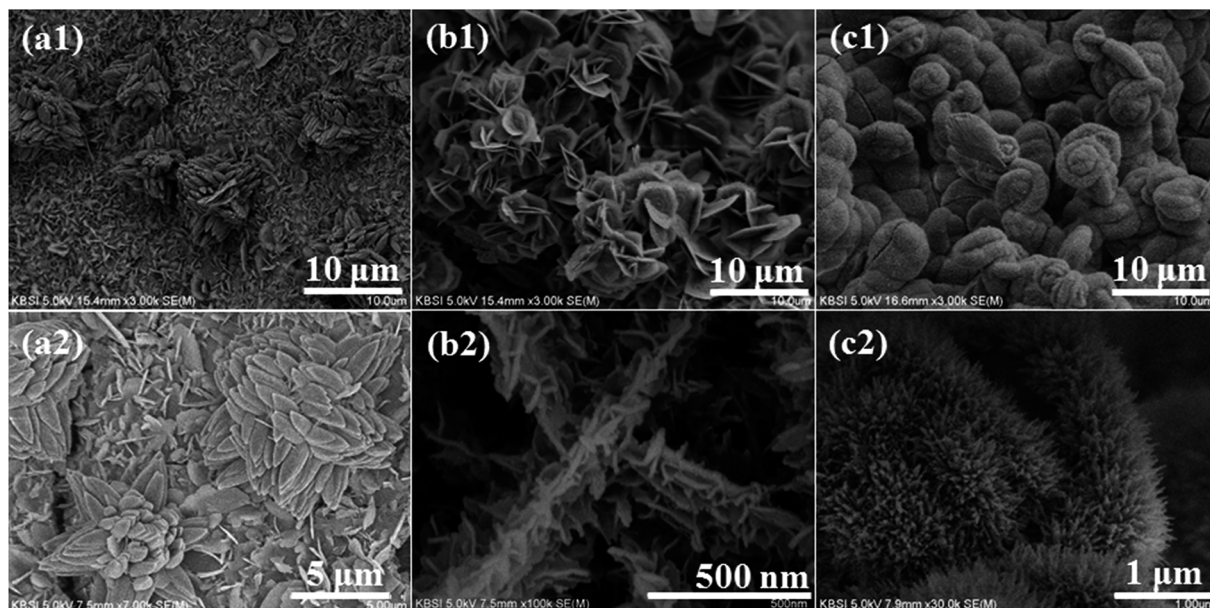
Fig. 1 (a1, b1 and c1) high magnification and (a2, b2 and c2) low magnification typical FE-SEM images of the (a1 and a2) MnO_2, (b1 and b2) $CoNiO_2$ and (c1 and c2) $MnO_2@CoNiO_2$ electrodes.

$MnO_2@CoNiO_2$ on the Ni-foam substrates. Fig. 1(a1 and a2) show FE-SEM images of the MnO_2 electrode, which had a nanoflower morphology with a uniform deposition. Fig. 1(b1 and b2) present low and high magnification SEM images of the as-synthesized nanoflakes, such as the $CoNiO_2$ sample. A low magnification FE-SEM of $MnO_2@CoNiO_2$ (Fig. 1(c1)) revealed uniform snail shell-like structure deposited on the Ni-foam. On the other hand, the high magnification FESEM image of $MnO_2@CoNiO_2$ (Fig. 1(c2)) showed the dense $CoNiO_2$ nanoneedles attached to the MnO_2. These novel nanostructured films provided an abundant porous surface area for contact between the electrolyte and electrode, which enhanced the performance of supercapacitors.

EDX was performed to determine the elemental distribution of the prepared electrodes. Fig. 2a–c present the EDX spectra of MnO_2, $CoNiO_2$ and $MnO_2@CoNiO_2$ electrodes, respectively. The EDX spectrum of MnO_2 revealed Mn and O, whereas $CoNiO_2$ exhibited Co, Ni, and O. On the other hand, the EDX spectrum of $MnO_2@CoNiO_2$ contained Co, Ni, Mn, and O, confirming that the $MnO_2@CoNiO_2$ had been deposited successfully on the surface of the Ni-foam. The crystal structures of the $MnO_2@CoNiO_2$ precursor was further studied using XRD analysis, as shown in Fig. 3. Besides the three strong peaks from the nickel foam substrate, the other diffraction peaks can be indexed to the (121) and (211) planes of the MnO_2 (JCPDS no. 14-0644) and the (111), (220) and (311) planes of the $CoNiO_2$ (JCPDS no. 10-0188), which is consistent with the previous literatures.[68,69]

XPS is one of the most useful and effective techniques for analyzing the surface composition and oxidation states of the elements. Fig. 4a presents the survey spectrum of the $MnO_2@CoNiO_2$ composite, indicating the existence of Co, Ni, O, C, and Mn. The high-resolution Co 2p spectrum (Fig. 4b) exhibited peaks at 781.8 eV and 797.15 eV for Co $2p_{3/2}$ and Co

$2p_{1/2}$, respectively.[70] These two oxidation states were separated by a 15.35 eV spin energy, which indicates Co^{+2}. The Ni 2p spectrum (Fig. 4c), showed two main spin–orbit peaks of Ni $2p_{3/2}$ at 856.24 eV and Ni $2p_{1/2}$ at 873.31 eV with a separation of approximately 17 eV, which is characteristic of Ni^{2+}.[71] The high resolution scan of Mn 2p of the composite (Fig. 4d) showed two peaks at 642.48 and 653.32 eV, which were assigned to Mn $2p_{3/2}$ and Mn $2p_{1/2}$, respectively, and the binding energy peaks of Mn 2p were separated by 10.84 eV. XPS confirmed that the $MnO_2@CoNiO_2$ composite consisted of Co^{2+}, Ni^{2+}, and Mn^{2+}.

To investigate the specific areas and the porous nature of the MnO_2, $CoNiO_2$ and $MnO_2@CoNiO_2$, BET gas sorption measurements were performed. The nitrogen adsorption/desorption isotherms and the pore size distribution plots of the three samples are shown in Fig. 5. Type IV isotherms were clearly exhibited, denoting the existence of mesopores in the three samples. The BET surface area of the prepared $MnO_2@CoNiO_2$ composite was obtained to be 40.6 m^2 g^{-1}, which was higher than that of the $CoNiO_2$ (27.3 m^2 g^{-1}) and MnO_2 (22.6 m^2 g^{-1}) samples. The pore size distribution curves from the N_2 adsorption isotherm of the Fe-SNC and SNC are shown in the inset of Fig. 5, it can be seen that $MnO_2@CoNiO_2$ has the pore size distribution of 20.1 nm, whereas MnO_2 and $CoNiO_2$ show pore sizes of 20.4 and 20.8 nm. These results indicate that the three samples are having mesoporous structures with large surface area that is much needed for the electrocatalytic applications.

CV was conducted in a 3 M KOH electrolyte over the potential range, 0.00 to 0.50 V at different scan rates of 5 to 100 mV s^{-1} for the MnO_2, $CoNiO_2$ and $MnO_2@CoNiO_2$ electrode materials, as shown in Fig. 6. Fig. 6a shows the CV curves of the three electrodes at a scan rate of 20 mV s^{-1} in a 3 M KOH electrolyte solution. The CV curve shape is different from the electric
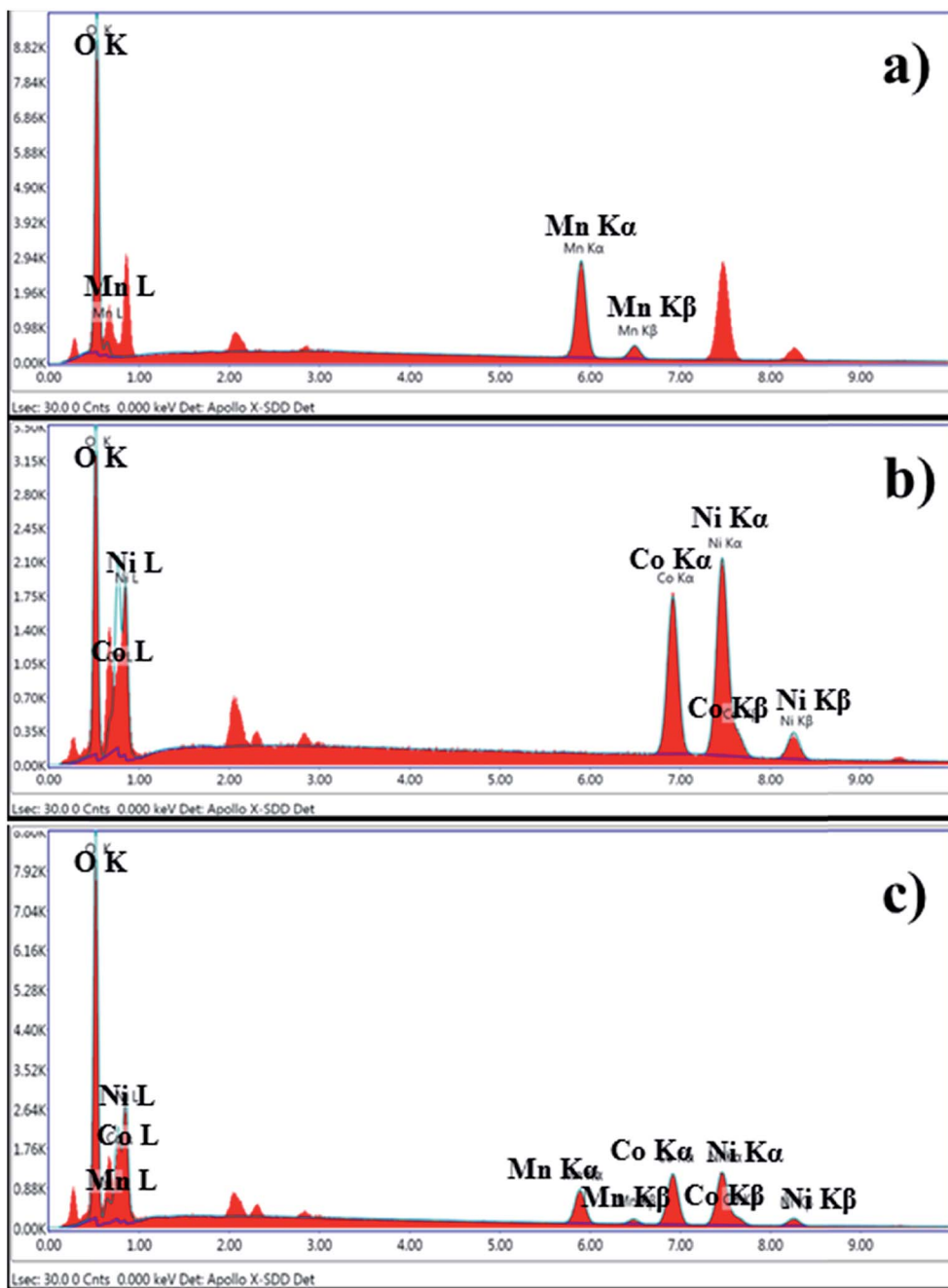
Fig. 2 EDX spectrum of (a) MnO_2, (b) $CoNiO_2$ and (c) $MnO_2@CoNiO_2$ electrodes on Ni-foam.

double-layer capacitance, showing that the capacitance was due mainly to the pseudo capacitive capacitance. Moreover, from the CV curve shapes, the integrated area of the $MnO_2@CoNiO_2$ electrode was higher than that of the other two electrode materials, showing that the $MnO_2@CoNiO_2$ electrode has the largest specific capacitance compared to the $CoNiO_2$ and MnO_2 electrodes. Fig. 6b and c shows a smaller surrounded area of $CoNiO_2$ and MnO_2 than that of the $MnO_2@CoNiO_2$ (Fig. 6d), suggesting the low electrochemical performance of $CoNiO_2$ and MnO_2.

Furthermore, the electrochemical performance of the electrodes was examined by galvanostatic charge–discharge (GCD)

tests. The GCD measurements were studied over the potential range, +0.0 V to +0.48 V, at different current densities (20 to 100 mA cm^{-2}). Fig. 7a–c show GCD plots of the MnO_2, $CoNiO_2$, and $MnO_2@CoNiO_2$ electrodes, respectively. The extracted specific capacitance of $MnO_2@CoNiO_2$ (Fig. 7d) were 1605.4, 1487.7, 1338.2, 1201.3, 1060.7, and 881.4 F g^{-1} at current densities of 20, 30, 40, 50, 60, and 100 mA cm^{-2}, respectively. The measured specific capacitances of $CoNiO_2$ were 1338.4, 1134.4, 1028.1, 970.8, 867.9, and 759.7 F g^{-1} at different current densities. Those of MnO_2 were 1069.0, 953.8, 810.1, 713.5, 593.7, and 482.0 F g^{-1} at different current densities. The specific
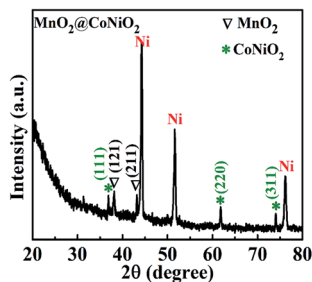
Fig. 3 XRD pattern of the $MnO_2@CoNiO_2$ on the surface of nickel foam substrate.

Fig. 5 The Brunauer–Emmett–Teller (BET) surface area measured from nitrogen adsorption–desorption isotherms and the insets show the corresponding pore-size distribution of the (a) MnO_2, (b) $CoNiO_2$ and (c) $MnO_2@CoNiO_2$ on Ni-foam substrate.

capacitance increased gradually with decreasing current density. The $MnO_2@CoNiO_2$ electrode showed a high specific capacitance of 1605.4 F g^{-1} at a current density of 20 mA cm^{-2}, whereas that of the $CoNiO_2$ and MnO_2 electrodes were only 1338.4 and 1069.0 F g^{-1} at the same current density. The excellent and superior specific capacitance of $MnO_2@CoNiO_2$ may be due to its higher surface area with the improved morphology of nanostructures. The power density and energy density are two essential parameters to examine the performance of supercapacitors. Fig. 8 shows the Ragone plots of MnO_2, $CoNiO_2$, and $MnO_2@CoNiO_2$. The $MnO_2@CoNiO_2$ exhibited a high energy density (51.37 W h kg^{-1}) and power density (1142.75 W kg^{-1}), which were much higher than those of the $CoNiO_2$ (42.83 W h kg^{-1} and 1599.95 W kg^{-1}) and MnO_2 (34.21 W h kg^{-1} and 1333.29 W kg^{-1}) at a current density of 20 mA cm^{-2}.

EIS is an efficient way to examine the electrochemical properties of electrodes; the impedance was measured over the frequency range, 100 mHz to 500 kHz, at a bias of 0 V, and the plots are shown in Fig. 9. All plots displayed a depressed
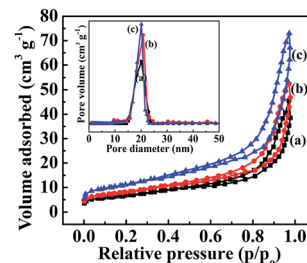
semicircle in the high-frequency region and a straight line in the low-frequency region. At high frequencies, the Z'-axis intercept indicated the equivalent series resistance (ESR) and the semicircle diameter was assigned to the charge transfer resistance (R_{ct}) at the interface of electrode/electrolyte. The ESR value of the $MnO_2@CoNiO_2$ electrode was smaller than that of the other two electrodes (MnO_2, $CoNiO_2$), which reflects the higher conductivity obtained in the $MnO_2@CoNiO_2$ electrode. On the other hand, as shown in the figure, a significant change in R_{ct} was observed after $MnO_2@CoNiO_2$ was added to the electrode material. According to the diameter of the semicircle, the R_{ct} of MnO_2, $CoNiO_2$, and $MnO_2@CoNiO_2$ electrodes were 27.3 Ω, 25.1 Ω, and 3.8 Ω, respectively, which shows that the $MnO_2@CoNiO_2$ composite can enhance the electronic conductivity and develop electron transfer at the interface of electrode material compared to MnO_2 and $CoNiO_2$ electrodes. The low ESR and R_{ct} of the $MnO_2@CoNiO_2$ electrode plays an important role in improving the performance of supercapacitors.
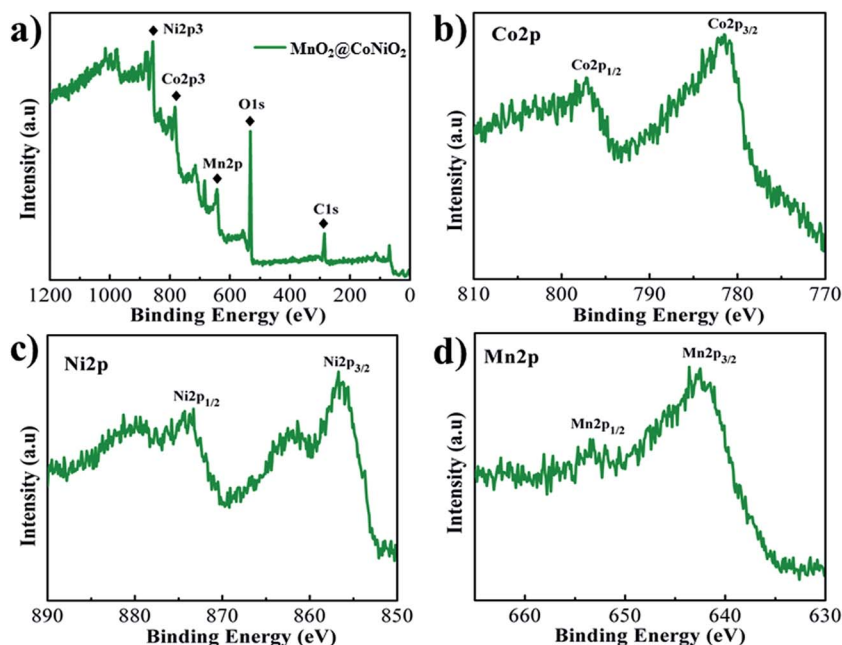

Fig. 4 XPS spectrum of $MnO_2@CoNiO_2$ on Ni-foam; (a) survey spectrum, high-resolution spectra for (b) Co 2p, (c) Ni 2p, and (d) Mn 2p.
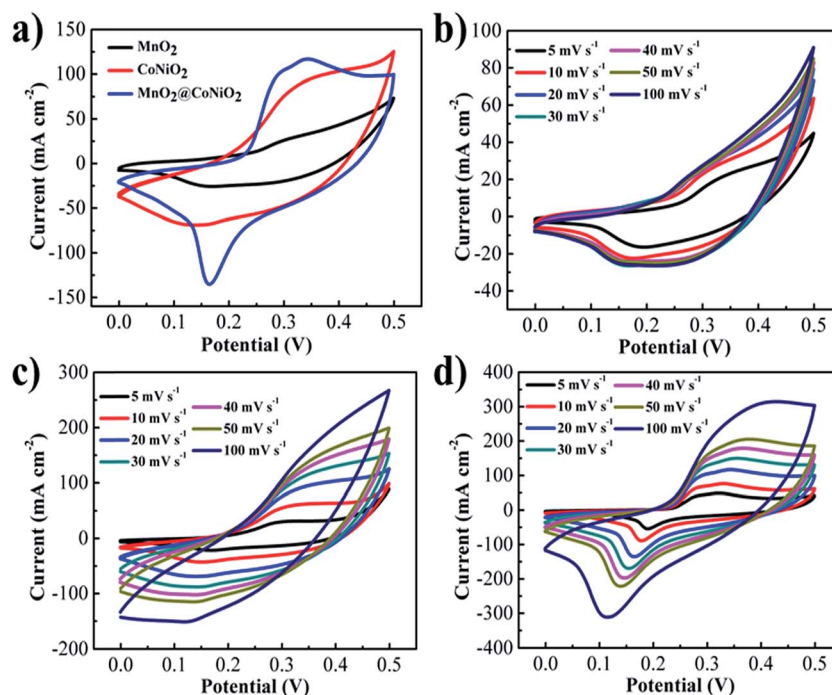
Fig. 6 (a) A comparison CV curves of the MnO_2, $CoNiO_2$ and $MnO_2@CoNiO_2$ electrodes at the scan rate of 20 mV s^{-1}. CV curves of the (b) MnO_2, (c) $CoNiO_2$ and (d) $MnO_2@CoNiO_2$ electrodes at different scan rates (5–100 mV s^{-1}) in 3 M KOH solution.

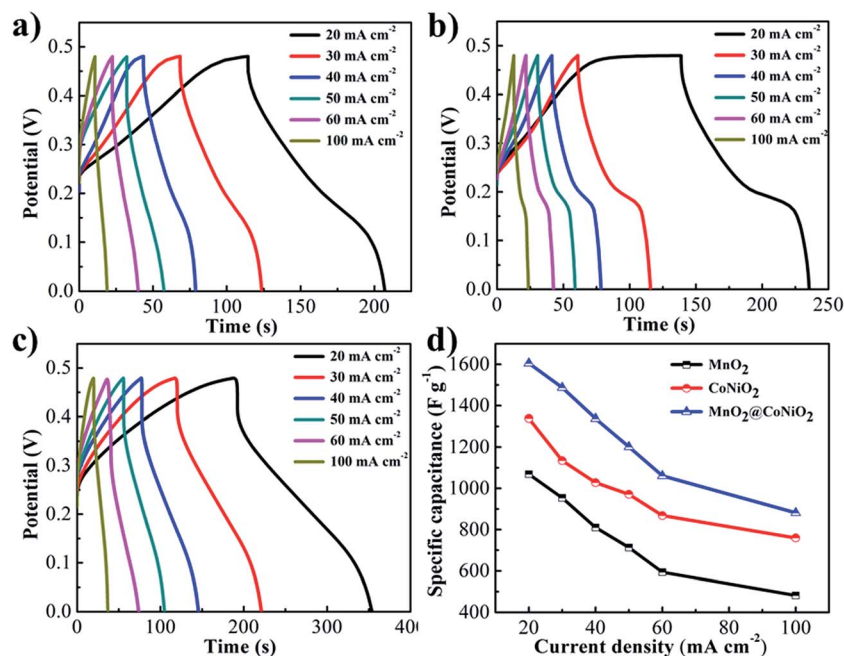**Fig. 7** Charge and discharge curves of the (a) MnO_2, (b) $CoNiO_2$ and (c) $MnO_2@CoNiO_2$ electrodes at different current densities (20–100 mA cm^{-2}) in 3 M KOH solution; (d) the measured specific capacitance as a function of current density.

The stability of the electrode materials is one of the most important requirements for supercapacitor applications. The cycling stability test of the MnO_2, $CoNiO_2$, and $MnO_2@CoNiO_2$ electrodes were evaluated at a constant charge–discharge current density of 40 mA cm^{-2} for 3000 cycles, as shown in

Fig. 10. The MnO_2 electrode for the 1st cycle showed a specific capacitance of 800.32 F g^{-1}, which decreased slowly to 762.36 F g^{-1} after 3000 cycles, showing 4.94% loss after 3000 cycles. The $CoNiO_2$ electrode showed specific capacitances of 1021.45 F g^{-1} and 998.56 F g^{-1} at the 1st cycle and after 3000 cycles,
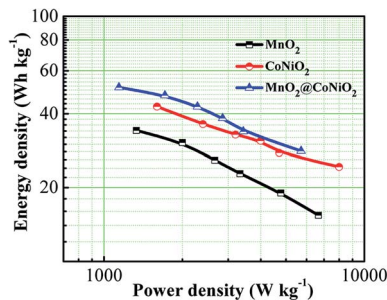
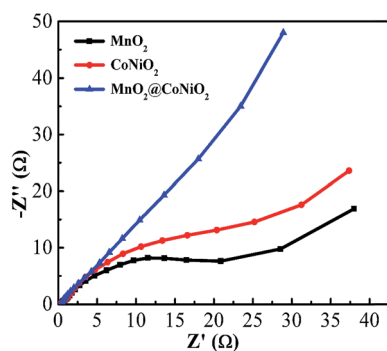**Fig. 8** Ragone plot of the MnO_2, $CoNiO_2$ and $MnO_2@CoNiO_2$ electrodes.

Fig. 9 Impedance Nyquist plots of the MnO_2, $CoNiO_2$ and $MnO_2@$-$CoNiO_2$ electrodes.
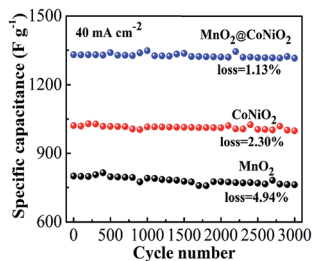

Fig. 10 Cyclic performance of the MnO_2, $CoNiO_2$ and $MnO_2@CoNiO_2$ electrodes at a current density of 40 mA cm^{-2} for 3000 cycles.

respectively, showing 2.30% loss after 3000 cycles. On the other hand, the $MnO_2@CoNiO_2$ electrode exhibited only 1.13% loss of a specific capacitance after more than 3000 cycles, highlighting the good long-term stability of the $MnO_2@CoNiO_2$ electrode.

4. Conclusions

In summary, novel $MnO_2@CoNiO_2$ snail shell-like structures were designed and synthesized using a simple hydrothermal method followed by annealing. The $MnO_2@CoNiO_2$ composite electrode exhibited superior specific capacitance (1605.4 F g^{-1}) and energy density (51.37 W h kg^{-1}), which were much higher than those of the MnO_2 (1069.0 F g^{-1}; 34.21 W h kg^{-1}) and $CoNiO_2$ (1338.4 F g^{-1}; 42.83 W h kg^{-1}) electrodes at a current density of 20 mA cm^{-2}. The elevated performance of the

composite electrode was attributed to the improved surface morphology with a high surface area, which facilitates electron diffusion at the contact between the electrode and electrolyte. Moreover, the $MnO_2@CoNiO_2$ electrode delivered outstanding cycling stability with a capacity retention of 98.87% after 3000 cycles (97.7% and 95.06% for the $CoNiO_2$ and MnO_2 electrodes after 3000 cycles, respectively). As a result, the $MnO_2@CoNiO_2$ composite electrode provides a path for high-performance supercapacitors because of its low-cost, facile preparation, and environmental friendliness.

Acknowledgements

References

1 B. Liu, D. Tan, X. Wang, D. Chen and G. Shen, *Small*, 2013, **9**, 1998–2004.

2 T. Chen, L. Qiu, Z. Yang, Z. Cai, J. Ren, H. Li, H. Lin, X. Sun and H. Peng, *Angew. Chem., Int. Ed.*, 2012, **51**, 11977–11980.

3 X. Lu, G. Wang, T. Zhai, M. Yu, S. Xie, Y. Ling, C. Liang, Y. Tong and Y. Li, *Nano Lett.*, 2012, **12**, 5376–5381.

4 B. Liu, B. Liu, Q. Wang, X. Wang, Q. Xiang, D. Chen and G. Shen, *ACS Appl. Mater. Interfaces*, 2013, **5**, 10011–10017.

5 T. Liu, Y. Ling, Y. Yang, L. Finn, E. Collazo, T. Zhai, Y. Tong and Y. Li, *Nano Energy*, 2015, **12**, 169–177.

6 C. Zhou, Y. Zhang, Y. Li and J. Liu, *Nano Lett.*, 2013, **13**, 2078–2085.

7 X. Wu, L. Jiang, C. Long, T. Wei and Z. Fan, *Adv. Funct. Mater.*, 2015, **25**, 1648–1655.

8 L. Yuan, X. H. Lu, X. Xiao, T. Zhai, J. Dai, F. Zhang, B. Hu, X. Wang, L. Gong, J. Chen, C. Hu, Y. Tong, J. Zhou and Z. L. Wang, *ACS Nano*, 2011, **6**, 656–661.

9 P. Simon and Y. Gogotsi, *Nat. Mater.*, 2008, **7**, 845–854.

10 C. Meng, C. Liu, L. Chen, C. Hu and S. Fan, *Nano Lett.*, 2010, **10**, 4025–4031.

11 T. Stimpfling and F. Leroux, *Chem. Mater.*, 2010, **22**, 974–987.

12 A. Burke, *J. Power Sources*, 2000, **91**, 37–50.

13 L. Yang, S. Cheng, Y. Ding, X. B. Zhu, Z. L. Wang and M. L. Liu, *Nano Lett.*, 2012, **12**, 321–325.

14 W. Zhou, X. Cao, Z. Zeng, W. Shi, Y. Zhu, Q. Yan, H. Liu, J. Wang and H. Zhang, *Energy Environ. Sci.*, 2013, **6**, 2216–2221.

15 L. Huang, D. Chen, Y. Ding, S. Feng, Z. L. Wang and M. Liu, *Nano Lett.*, 2013, **13**, 3135–3139.

16 T. Zhu, J. S. Chen and X. W. Lou, *J. Mater. Chem.*, 2010, **20**, 7015–7020.

17 B. Wang, T. Zhu, H. B. Wu, R. Xu, J. S. Chen and X. W. Lou, *Nanoscale*, 2012, **4**, 2145–2149.

18 Q. Wang, X. Wang, B. Liu, G. Yu, X. Hou, D. Chen and G. Shen, *J. Mater. Chem. A*, 2013, **1**, 2468–2473.

19 M. Huang, Y. Zhang, F. Li, L. Zhang, R. S. Ruoff, Z. Wen and Q. Liu, *Sci. Rep.*, 2014, **4**, 3878.

20 M. Huang, R. Mi, H. Liu, F. Li, X. L. Zhao, W. Zhang, S. X. He and Y. X. Zhang, *J. Power Sources*, 2014, **269**, 760–767.

21 T. Brezesinski, J. Wang, S. H. Tolbert and B. Dunn, *Nat. Mater.*, 2010, **9**, 146–151.

22 Z. Lu, Z. Chang, W. Zhu and X. Sun, *Chem. Commun.*, 2011, **47**, 9651–9653.

23 M. Huang, Y. Zhang, F. Li, L. Zhang, Z. Wen and Q. Liu, *J. Power Sources*, 2014, **252**, 98–106.

24 L. Yu, B. Guan, W. Xiao and X. W. Lou, *Adv. Energy Mater.*, 2015, **5**, 1500981.

25 P. M. DiCarmine, T. B. Schon, T. M. McCormick, P. P. Klein and D. S. Seferos, *J. Phys. Chem. C*, 2014, **118**, 8295–8307.

26 N. Kundakarla, S. Lindeman, M. H. Rahman and M. D. Ryan, *Inorg. Chem.*, 2016, **55**, 2070–2075.

27 Y. Zhao, L. Hu, S. Zhao and L. Wu, *Adv. Funct. Mater.*, 2016, **26**, 4085–4093.

28 D. Cai, D. Wang, B. Liu, L. Wang, Y. Liu, H. Li, Y. Wang, Q. Li and T. Wang, *ACS Appl. Mater. Interfaces*, 2014, **6**, 5050–5055.

29 J. Xu, Q. Wang, X. Wang, Q. Xiang, B. Liang, D. Chen and G. Shen, *ACS Nano*, 2013, **7**, 5453–5462.

30 Y. Wu, G. Gao and G. Wu, *J. Mater. Chem. A*, 2015, **3**, 1828–1832.

31 W. Zhou, D. Kong, X. Jia, C. Ding, C. Cheng and G. Wen, *J. Mater. Chem. A*, 2014, **2**, 6310–6315.

32 W. Tang, L. Liu, S. Tian, L. Li, Y. Yue, Y. Wu and K. Zhu, *Chem. Commun.*, 2011, **47**, 10058–10060.

33 L. Hou, C. Yuan, L. Yang, L. Shen, F. Zhang and X. Zhang, *RSC Adv.*, 2011, **1**, 1521–1526.

34 L. Zhu, W. Wu, Y. Zhu, W. Tang and Y. Wu, *J. Phys. Chem. C*, 2015, **119**, 7069–7075.

35 X. Lu, G. Wang, T. Zhai, M. Yu, J. Gan, Y. Tong and Y. Li, *Nano Lett.*, 2012, **12**, 1690–1696.

36 R. Li, X. Ren, F. Zhang, C. Du and J. Liu, *Chem. Commun.*, 2012, **48**, 5010–5012.

37 L. Zhu, Z. Chang, Y. Wang, B. Chen, Y. Zhu, W. Tang and Y. Wu, *J. Mater. Chem. A*, 2015, **3**, 22066–22072.

38 R. Tummala, R. K. Guduru and P. S. Mohanty, *J. Power Sources*, 2012, **209**, 44–51.

39 F. Li, Y. X. Zhang, M. Huang, Y. Xing and L. L. Zhang, *Electrochim. Acta*, 2015, **154**, 329–337.

40 S. J. Zhu, J. Zhang, J. J. Ma, Y. X. Zhang and K. X. Yao, *J. Power Sources*, 2015, **278**, 555–561.

41 M. Huang, F. Li, F. Dong, Y. X. Zhang and L. L. Zhang, *J. Mater. Chem. A*, 2015, **3**, 21380–21423.

42 J. G. Wang, F. Kang and B. Wei, *Mater. Sci.-Pol.*, 2015, **74**, 51–124.

43 J. Zhu, S. Tang, H. Xie, Y. Dai and X. Meng, *ACS Appl. Mater. Interfaces*, 2014, **6**, 17637–17646.

44 Y. He, W. Chen, X. Li, Z. Zhang, J. Fu, C. Zhao and E. Xie, *ACS Nano*, 2013, **7**, 174–182.

45 G. Q. Zhang and X. W. Lou, *Adv. Mater.*, 2013, **25**, 976–979.

46 T. Y. Wei, C. H. Chen, H. C. Chien, S. Y. Lu and C. C. Hu, *Adv. Mater.*, 2010, **22**, 347–351.

47 C. Z. Yuan, J. Y. Li, L. R. Hou, L. Yang, L. F. Shen and X. G. Zhang, *J. Mater. Chem.*, 2012, **22**, 16084–16090.

48 L. L. Li, Y. L. Cheah, Y. Ko, P. Teh, G. Wee, C. L. Wong, S. J. Peng and M. Srinivasan, *J. Mater. Chem. A*, 2013, **1**, 10935–10941.

49 Y. Liu, Y. Zhao, Y. Yu, M. Ahmad and H. Sun, *Electrochim. Acta*, 2014, **132**, 404–409.

50 Z. J. Fan, J. Yan, L. J. Zhi, Q. Zhang, T. Wei, J. Feng, M. Zhang, W. Qian and F. Wei, *Adv. Mater.*, 2010, **22**, 3723–3728.

51 B. G. Choi, M. Yang, W. H. Hong, J. W. Choi and Y. S. Huh, *ACS Nano*, 2012, **6**, 4020–4028.

52 J. Han, M. Wang, S. Cao, P. Fang, S. Lu, R. Chen and R. Guo, *J. Mater. Chem. A*, 2013, **1**, 13197–13202.

53 J. Zhi, O. Reiser, Y. Wang and A. Hu, *Nanoscale*, 2016, **8**, 11976–11983.

54 J. Zhou, H. Zhao, X. Mu, J. Chen, P. Zhang, Y. Wang, Y. He, Z. Zhang, X. Pan and E. Xie, *Nanoscale*, 2015, **7**, 14697–14706.

55 H. Chen, M. Zhou, T. Wang, F. Li and Y. X. Zhang, *J. Mater. Chem. A*, 2016, **4**, 10786–10793.

56 M. Huang, X. L. Zhao, F. Li, W. Li, B. Zhang and Y. X. Zhang, *J. Mater. Chem. A*, 2015, **3**, 12852–12857.

57 A. Ramadoss and S. J. Kim, *Int. J. Hydrogen Energy*, 2014, **39**, 12201–12212.

58 Z. Sun, W. Ai, J. Liu, X. Qi, Y. Wang, J. Zhu, H. Zhang and T. Yu, *Nanoscale*, 2014, **6**, 6563–6568.

59 Z. C. Xing, Q. X. Chu, X. B. Ren, C. J. Ge, A. H. Qusti, A. M. Asiri, A. O. Al-Youbi and X. P. Sun, *J. Power Sources*, 2014, **245**, 463–467.

60 C. V. V. M. Gopi, M. V. Haritha, S. K. Kim, K. Prabakara and H. J. Kim, *RSC Adv.*, 2016, **6**, 102961–102967.

61 X. Tang, R. Jia, T. Zhai and H. Xia, *ACS Appl. Mater. Interfaces*, 2015, **7**, 27518–27525.

62 J. Liu, J. Jiang, C. Cheng, H. Li, J. Zhang, H. Gong and H. J. Fan, *Adv. Mater.*, 2011, **23**, 2076–2081.

63 S. Zhang, S. Wang and S. Li, *Nanotechnology*, 2010, **10**, 5612–5617.

64 W. Ma, H. Nan, Z. Gu, B. Geng and X. Zhang, *J. Mater. Chem. A*, 2015, **3**, 5442–5448.

65 L. Yu, G. Zhang, C. Yuan and X. W. Lou, *Chem. Commun.*, 2013, **49**, 137–139.

66 Z. Gu, R. Wang, H. Nan, B. Geng and X. Zhang, *J. Mater. Chem. A*, 2015, **3**, 14578–14584.

67 S. Yang, P. Yan, Y. Li, K. Cheng, K. Ye, C. Zhang, D. Cao, G. Wang and Q. Li, *RSC Adv.*, 2015, **5**, 87521–87527.

68 P. Sun, H. Yi, T. Peng, Y. Jing, R. Wang, H. Wang and X. Wang, *J. Power Sources*, 2017, **341**, 27–35.

69 J. Zhang, Z. Chen, Y. Wang and H. Li, *Energy*, 2016, **113**, 943–948.

70 D. Li, Y. Gong and C. Pan, *Sci. Rep.*, 2016, **6**, 29788.

71 Y. Liu, Y. Zhao, Y. Yu, J. Li, M. Ahmad and H. Sun, *New J. Chem.*, 2014, **38**, 3084–3091.